AIChE

Bubble Evolution and Necking at a Submerged Orifice for the Complete Range of Orifice Tilt

Arup K. Das and Prasanta K. Das
Dept. of Mechanical Engineering, Indian Institute of Technology, Kharagpur 721302, India

DOI 10.1002/aic.13828

Bubble formation at an inclined orifice has been studied numerically using coupled-diffused interface-smoothed particle hydrodynamics. The simulation covers the entire range of orifice inclination, starting from upward facing (0°) to downward facing (180°) orientation for a moderate air flow (30 cm^3/s). Bubble at the orifice mouth becomes asymmetric as the plate gets tilted. The asymmetry maximizes at vertical orientation but with downward facing orifices symmetry restores. The local hydrodynamic structure reveals that the internal circulation cells in bubble become stronger as the inclination increases making the growing bubble asymmetric. Interestingly, bubble volume for downward facing orifice is 4.75 times higher than the bubble released at upward facing orifice. Observations from the present simulations suggest that bubble frequency and shape can be controlled by allowing appropriate inclination in the orifice mouth. © 2012 American Institute of Chemical Engineers *AIChE J,* 59: 630–642, 2013

Keywords: submerged orifice, orifice inclination, bubble, frequency, smoothed particle hydrodynamics

Introduction

Formation of bubbles at submerged orifices, its subsequent growth and finally its departure from the orifice mouth, comprises a number of complex hydrodynamic processes. This phenomenon finds a wide application in a variety of chemical and process equipment. The evolution of bubble at the orifice mouth can be subdivided into two different periods, namely initial and final growth period. Air bubbles form at the orifice mouth initially as a part of a sphere and grow further as time progresses. At the final stage, the bubble becomes elongated and its shape no longer remains spherical. Rather, at the advanced stage of the growth, a neck is formed adjacent to the orifice plane. Narrowing of the neck leads to the subsequent detachment of the bubble. The physics behind the phenomena is quite complex and over the years, a volume of investigations have been made to understand, analyze, and predict it. Researchers have taken the recourse of all the available avenues of investigation namely experimental, analytical, and lately computational to study the process of bubbling through submerged orifices.

Davidson and Schuler[1,2] first attempted to understand the phenomenon of bubbling in both water and mineral oil from 0.16- to 7.9-mm orifice diameters through experimental investigations. Later, several researchers[3–5] tracked the bubble shape and frequency of bubble departure for different surrounding fluids. Kulkarni and Joshi[6] reported an elaborate review of the previous experimental works related to bubble evolution from submerged orifice. Many investigations have also been reported for bubble formation process in microgravity situation. Kim et al.,[7] Pamperin and Rath,[8] Buyevich and Webbon,[9] and Chakraborty et al.[10] made continuous efforts to understand the interface evolution under different levels of microgravity. Three different bubble regimes namely static, dynamic, and turbulent regimes are observed during bubbling under microgravity. After the initial studies made by Davidson and Schuler,[1] researchers have proposed a large number of models to describe the phenomenon. Theoretical studies by Ramakrishnan et al.,[11] McCann and Prince,[4] Marmur and Rubin,[12] Oguz and Prosperetti,[13] Zhang and Tan,[14] and Xiao and Tan,[15] to name a few, provided different theoretical models. Simultaneously, efforts were also made to assess the effect of the influencing parameters like liquid properties,[1,16–21] gas properties,[22,23] chamber volume,[24,25] and orifice construction[26–28] on the process of bubble formation from a submerged orifice.

With the advancement of computational techniques, researchers tried to model the bubble formation phenomena numerically and understand the local hydrodynamic structures. In this regard, the contribution of Durst and coworkers[29–31] is worth mentioning. They have used volume of fluid (VOF) and combined VOF and level set (LS) techniques to capture the dynamic bubble profile. The efforts reported above are positive steps toward the development of the knowledge about the bubble formation process from a submerged orifice. Recently, Das and Das[32,33] have demonstrated that Lagrangian-smoothed particle hydrodynamics (SPH) could be an efficient computational technique for simulating the spatiotemporal development of bubbles at submerged orifices. SPH enjoys the edge over traditional grid-based methods due to its simple physical interpretation. The discretization scheme adapted by SPH reduces the governing equations to a system of ordinary differential equations that essentially represents the simple Newton's

---

Correspondence concerning this article should be addressed to P. K. Das at pkd@mech.iitkgp.ernet.in.

Second Law of motion for each particle. As a result, with a reasonably less computational effort, different physical effects can be incorporated through pairwise molecular-type interactions. Moreover, the particle formulation conserves mass, momentum, and energy as the total number of particles remain constant throughout a simulation. SPH became an obvious choice for many multiphase simulation, as it handles geometrically complex boundaries, contact line dynamics, and complex fluid–fluid interface dynamics efficiently and with ease in comparison to the traditional grid-based methods. This has been well established by simulating complex pinch off process of bubble over orifice mouth.[32]

But, all the experimental efforts reported symmetric bubbles at the orifice and the developed models accounted the formation, growth, and departure of nonspherical symmetric bubbles over the orifice mouth. However, asymmetry in bubble shape is not uncommon. Bubble nucleation due to phase change and chemical reaction over inclined surface can generate asymmetric bubble. During the production of aluminum, fluorine, or hydrogen, asymmetric bubble release pattern along the vertical or inclined electrodes are quite essential[34–36] to avoid gas accumulation at the nucleation site. Numerical simulation of such phenomenon can provide the insights regarding the formation and sliding of bubbles over inclined surfaces. The generated bubbles become asymmetric when the orifice plane is inclined to the horizontal as well as under the influence of cross flow even for a horizontal orifice plate. Bubble formation from an orifice mouth under cross flow situation is very common and some investigations have already been made by the researchers[37–39] for understanding the change of shape for different shear strength. But, the effect of orifice inclination has not yet been considered comprehensively. To the best of the knowledge of the authors, the only effort in this direction is made by Kumar and Kuloor.[40] Nevertheless, there is a great need to understand the effect of orifice inclination on the change of bubble volume, its contour, and departure frequency. Orifice inclination can have a profound effect on the hydrodynamics of bubbling as it destroys the symmetry and renders bubbles three dimensional (3-D). Such a problem is not easily amenable through analytical treatment. When the bubbles are not axisymmetric, even experiment or the numerical simulation becomes challenging. To have an insight into the bubble formation, its growth, departure, or sliding over inclined surfaces as well as the associated hydrodynamics of the surrounding liquid, it is necessary to use a 3-D computational simulation.

In this work, diffuse interface (DI)-based Lagrangian SPH has been adopted to simulate bubble formation from an inclined orifice. DI has been adopted in many computational algorithms for a better simulation of the property variation across the complex interface. DI has been successfully implemented in the conventional grid-based formulations[41–43] and in the Lattice Boltzmann method.[44] Recently, its application has been extended to SPH.[45] The improvements that can be achieved by incorporating DI in the basic SPH has been demonstrated by Das and Das.[32,33] The present selection of the computational algorithm for the simulation of the 3-D process of bubbling from a submerged orifice is based on these studies.

Air and water at atmospheric pressure and temperature are used as the working fluids in the simulations. It is assumed that air is injected with a constant air flow rate (30.0×10^{-6} m^3/s) from the orifice in a quiescent water column. The objective of the present work is to investigate the formation, growth, pinching, and detachment of the bubble from an inclined orifice of radius 1.5×10^{-3} m under normal gravity. Injected bubble is assumed to be pinned with the orifice mouth. Inclination angle of the orifice plate is varied from 0° to 180° with respect to horizontal. Bubble contour at different time instant for different inclination angle of the orifice plate is reported along with the bubble frequency and its volume during departure. With the help of Lagrangian particle history, the velocity fields in the gas and the liquid phase are investigated during the growth and departure of the bubble. Finally, a study has been made to understand the process of neck formation and pinching of the asymmetric bubbles at the orifice mouth.

Formulation of the Problem

Computational domain

Because of the complexity of the problem, the computational domain and coordinate system need to be selected carefully. A 3-D domain filled with water under atmospheric pressure is considered. Air enters the liquid domain at constant velocity through a constant diameter orifice fixed on a straight solid plane. The plane of the orifice defines one of the boundaries of the computational domain. To simulate the bubbling from the orifice over the entire range of inclination, three different orientations of the orifice plane $0^\circ < \alpha_1 < 90^\circ$ (Figure 1a), $\alpha_1 = 90^\circ$ (Figure 1b), and $180^\circ > \alpha_1 > 90^\circ$ (Figure 1c) have been considered. A 3-D cylindrical coordinate system (r–θ–z) is adopted. An additional local coordinate system (x_1–x_2) is also placed at the orifice mouth pointing toward the bulk fluid for a convenient description of the growing bubbles. An exaggerated view of the DI is also shown in the figure. Two different types of particles are located at the bulk phases of air and water domain and the DI is denoted by the particles of intermediate colors of the bulk phases.

Governing equations

The basic conservation equations for mass and momentum equations are described below:

Mass conservation equation is as follows considering both the phases are incompressible

$$\nabla.\vec{V} = 0. \tag{1}$$

With the incorporation of the DI, the momentum conservation equation can be expressed as

$$\rho\left(\frac{\partial \vec{V}}{\partial t} + \nabla.\vec{V}\vec{V}\right) = -\nabla P + \rho\vec{g} + \nabla.\tau + \sigma_{lv}k\vec{n}\delta_s - \frac{C}{Ca.Cn}\nabla\phi. \tag{2}$$

The interface between the phases is considered to be small but of finite thickness (ξ). Last term of Eq. 2 signifies the change of surface energy in the region of DI whereas the penultimate term signifies the surface tension force acting toward normal of the interface. In the above equation, the gradients of scalar f (pressure and chemical potential) and vector A (velocity and gravity) can be written as $\nabla f = \frac{\partial f}{\partial r}\hat{r} + \frac{1}{\rho}\frac{\partial f}{\partial \theta}\hat{\theta} + \frac{\partial f}{\partial z}\hat{z}$ and $\nabla.\vec{A} = \frac{1}{\rho}\frac{\partial(\rho A_r)}{\partial r} + \frac{1}{\rho}\frac{\partial A_\theta}{\partial \theta} + \frac{\partial A_z}{\partial z}$. $\vec{V}$, $\vec{n}$, and P are the velocity vector, unit normal vector at the interface, and pressure, respectively. To differentiate two different types of fluid

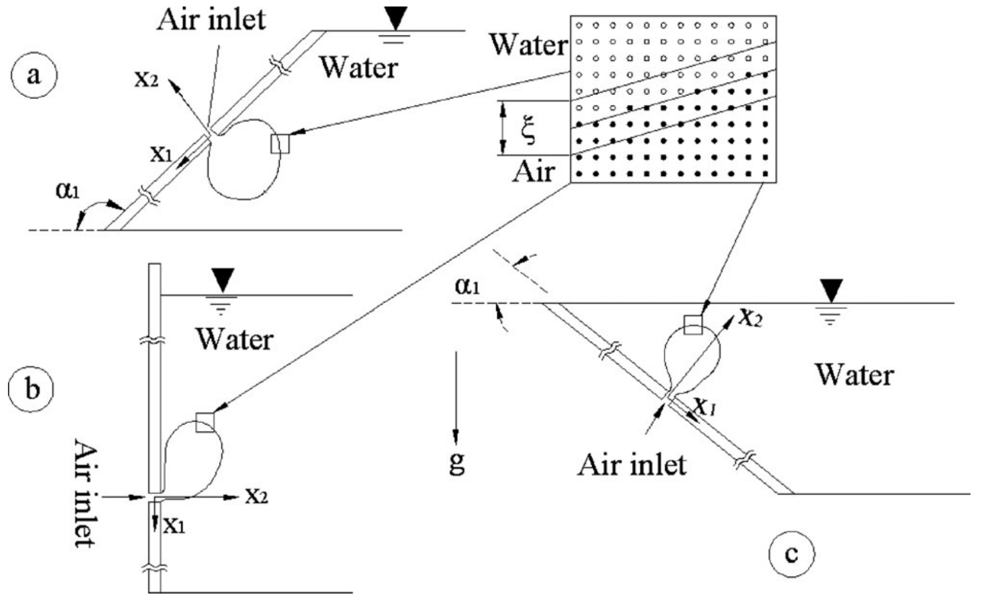

Figure 1. Schematic diagram for the orientation of the orifice and the local coordinate system.

(a) $\alpha 1 < 90°$, (b) $\alpha 1 = 90°$, and (c) $\alpha 1 > 90°$.

particles from each other, a color code (C) has been assigned with $+1$ value for the liquid and -1 for the gas. Phase gradient energy across the interface is considered by defining chemical potential as

$$\phi = \left[\nabla(C+1)^2(C-1)^2 - \left(C_{\mathrm{n}}{}^2\nabla^2 C\right)\right]. \tag{3}$$

In the case of multiphase flow, chemical potential ϕ is defined as the change in discrete Helmholtz free energy upon addition of an amount of one-phase, keeping temperature, volume, and other phase density distributions fixed. Here, C_{n} is the ratio of mean interfacial thickness (ξ) and characteristics length scale (orifice diameter). σ_{lv}, τ, k, and δ_{s} are the gas–liquid surface tension, shear stress, curvature of the interface, and surface delta function, respectively. Capillary number (Ca) is the ratio of viscous and surface forces.

To discretize the system of equations mentioned above, Lagrangian particle-based DI-SPH is used. DI-SPH uses its inherent advantage of particle-based formulation to track the spatiotemporal development of the interface. Both the gaseous and liquid domains are discretized by a number of ordered particles. Each of the phases contains a specific type of particle characterized by mass m_i and density ρ_i. Furthermore, all the particles will have their respective velocity v_i.

Evolution of thermophysical properties and parameters like velocity and density of all the particles are updated depending on the weighted average of these properties of all the neighboring particles. Neighbors of one particle are determined using "all particle search" procedure within a smoothing length (h). The dependence of the neighbors over the particle of interest is evaluated based on the scalar distance between the particles. Using discretization of SPH (Annexure 1), the continuity and momentum equation can be described as

$$\rho_i = \frac{\sum_{j=1}^{N} m_j W_{ij}}{\sum_{j=1}^{N}\left(\frac{m_j}{\rho_j}\right) W_{ij}} \tag{4}$$

$$\begin{aligned}\frac{Dv_i^{\alpha}}{Dt} &= \sum_{j=1}^{N} m_j \left(\frac{\sigma_i^{\alpha\beta} + \sigma_i^{\alpha\beta}}{\rho_i\rho_j} + \xi_{ij}\right)\frac{\partial W_{ij}}{\partial x_i^{\beta}} \\ &+ \sum_{j=1}^{N} m_j\overline{g} - \sum_{j=1}^{N}\frac{m_j}{\rho_i\rho_j}\frac{\left(\frac{C_i}{Ca_iCn_i} + \frac{C_j}{Ca_jCn_j}\right)\left(\phi_i - \phi_j\right)}{\left|r_{ij}\right|}\frac{\partial W_{ij}}{\partial r_{ij}}\end{aligned} \tag{5}$$

Here, α is the prime index and β is the dummy index which can be any coordinate other than α. In Eq. 5, Ca is the capillary number ($ca_{ij} = v_i\mu_{ij}/\sigma_{ij}$) and $\sigma_i^{\alpha\beta}$ is the stress tensor[46] (Annexure 2).

After placing the particles into its new position depending on the velocity vector and time step (Δt), the chemical potential (ϕ_i) and color code (C_i) are updated using simultaneous Cahn–Hilliard equation[41] (Annexure 2).

To couple pressure field with density field of the discretized particle-based system, following equation is applied:

$$p_i = B\left(\left(\frac{\rho_i}{\rho_0}\right)^7 - 1\right). \tag{6}$$

Apart from the bulk momentum transfer, surface tension force is applied across the DI following the continuum surface force (CSF) method.[47] For details, one can refer Annexure 3.

Boundary and initial conditions

The liquid and gaseous phase is bounded by solid walls having no slip and penetration boundary conditions. To model the solid boundary, two layers of boundary particles are placed along the wall. The model assumes perfectly smooth solid surface. Boundary particles pose a resistive force to the interior fluid particles to restrict them to penetrate and slip over the solid boundaries. The resistive force is similar in nature to the interfacial no penetration force as has been mentioned in Eq. 13.

Air and water at atmospheric pressure (101 kPa) and temperature (293 K) are assumed to be the fluid in consideration. The surface tension between air and water is considered to be 72.8×10^{-3} N/m. DI concept helps to handle property jump across the interface having viscosity ratio 55 and

Table 1. Effect of Particle Spacing on Bubble Volume

Number of Particle Per Millimeter	Bubble Volume During Departure (cm^3/s)
4	0.437
6	0.451
10	0.459
15	0.461

density ratio 840. As the purpose of the investigation is to study the effect of orifice inclination, simulations have been made for a single orifice diameter of 3 mm and a single gas flow rate of 30 cm^3/s. This makes the flow Reynolds number ($\mathrm{Re} = \frac{2\rho_l Q}{\mu_l D_o}$) and capillary number ($\mathrm{Ca} = \frac{4\mu_l Q}{\sigma D_o^2}$) to be 19,922 and 0.18, respectively. As the simulation is made for normal gravity, Bond number ($\mathrm{Bo} = \frac{\rho_l g D_o^2}{4\sigma}$) is considered to be in the order of 0.3.

Numerical procedure

At any time step, the particles are allowed to take their own position obeying the continuity (Eq. 3) and momentum equation (Eqs. 4 and 5) under the influence of gravity and surface tension. At the newly obtained positions of the particles, the color and chemical potential are updated using Eqs. 8 and 9, respectively. Before going to the next time instant, a check has been made for sudden penetration of particles into the boundary particles. The simulation continues until the bubble detaches from the orifice mouth.

Number of iterations varies depending on the bubble size which in turn depends on the inclination angle of the orifice plate. At the beginning of the simulation, the particles are placed uniformly in the domain. Initial density of the particles is chosen through a rigorous spacing independence test. Table 1 shows the bubble volume at departure for different particle spacing. It may be noted that the results presented in this table are for an orifice diameter of 5.945 mm and an air flow of 9.21 cm^3/s which is identical to the parameters considered by Ramakrishnan et al.[11] It can be observed that the difference between the bubble volume with 6 and 10 particles per millimeter is -1.74%. Conversely, if the number of particles per millimeter is increased from 10 to 15, the difference in bubble volume is only 0.43%. Based on this, it has been decided that 10 particles will be accommodated per millimeter in all the directions for optimum spacing. For the present simulation, forward marching is done in time with a step of 10^{-4} s to get a steady dynamics solution. Computation time always depends on the inclination angle and flow rate. For a Pentium IV (3 GB RAM) computer, the average CPU time is around 15 min.

Validation

Das and Das[32] rigorously validated basic SPH scheme for a problem of bubbling at a submerged orifice. Subsequently, they have incorporated the concept of DI within the framework of SPH[32] and validated their simulation of bubbling through a horizontal orifice against the work of Gerlach et al.[29] and Zhang and Shoji,[48] while the first one is a computational simulation using combined LS and VOF and the other one is an experimental investigation. The DI-SPH simulation exhibited very close agreement with both the results. DI-SPH simulation can successfully simulate both the process of bubbling at the orifice and the motion of the bubble after detachment.

Furthermore, validation is reported in Figure 2a for the bubble volume at the point of detachment over a range of flow rate for an orifice diameter of 5.945 mm. Experimental observations of Ramakrishnan et al.[11] are compared with our prediction for a horizontal orifice plate. Air flow rate from 1.5 to 80 cm^3/s is considered during the simulation. The developed model records 2.8% maximum error in predicting the bubble volume at the instant of departure from the orifice mouth.

For the same conditions,[11] equivalent spherical radius of the generated bubbles is reported in Figure 2b. Numerical results from the simulation are compared very well (3.6% maximum error) with a generalized correlation proposed by Jamialahmadi et al.[49] They have derived their correlations through a rigorous analysis using 900 data points covering a wide range of operating parameters. Agreement of the developed model with such generalized correlations shows the applicability of the developed model.

Results and Discussions

Observations from numerical simulations are discussed in this section. Efforts have also been made to analyze the results obtained from the simulations.

Bubble growth history

The aim of the present work is to simulate bubble formation from an inclined orifice mouth submerged in a quiescent liquid pool under constant flow condition and to study the

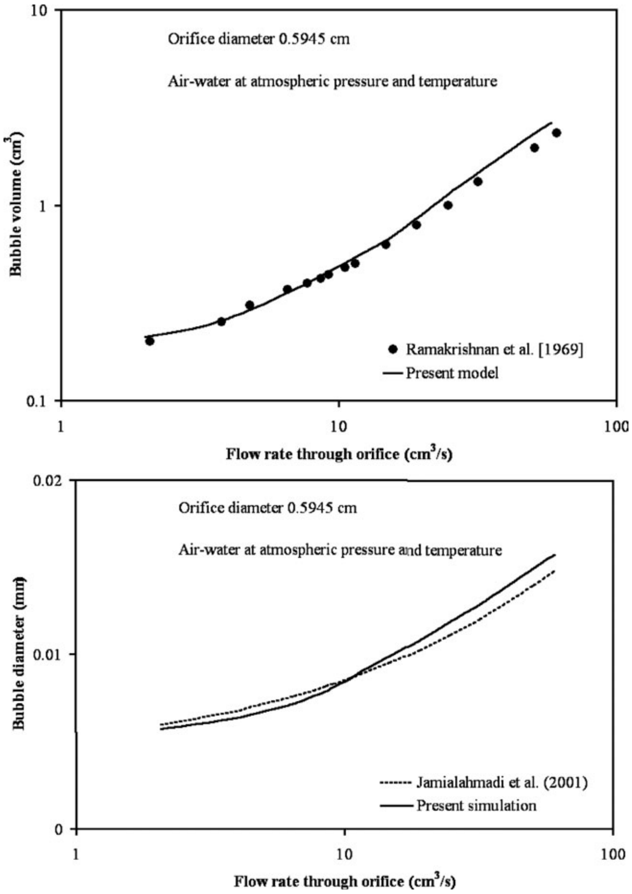

Figure 2. Comparison of bubble volume and diameter during departure for different flow rate through the orifice with literature.

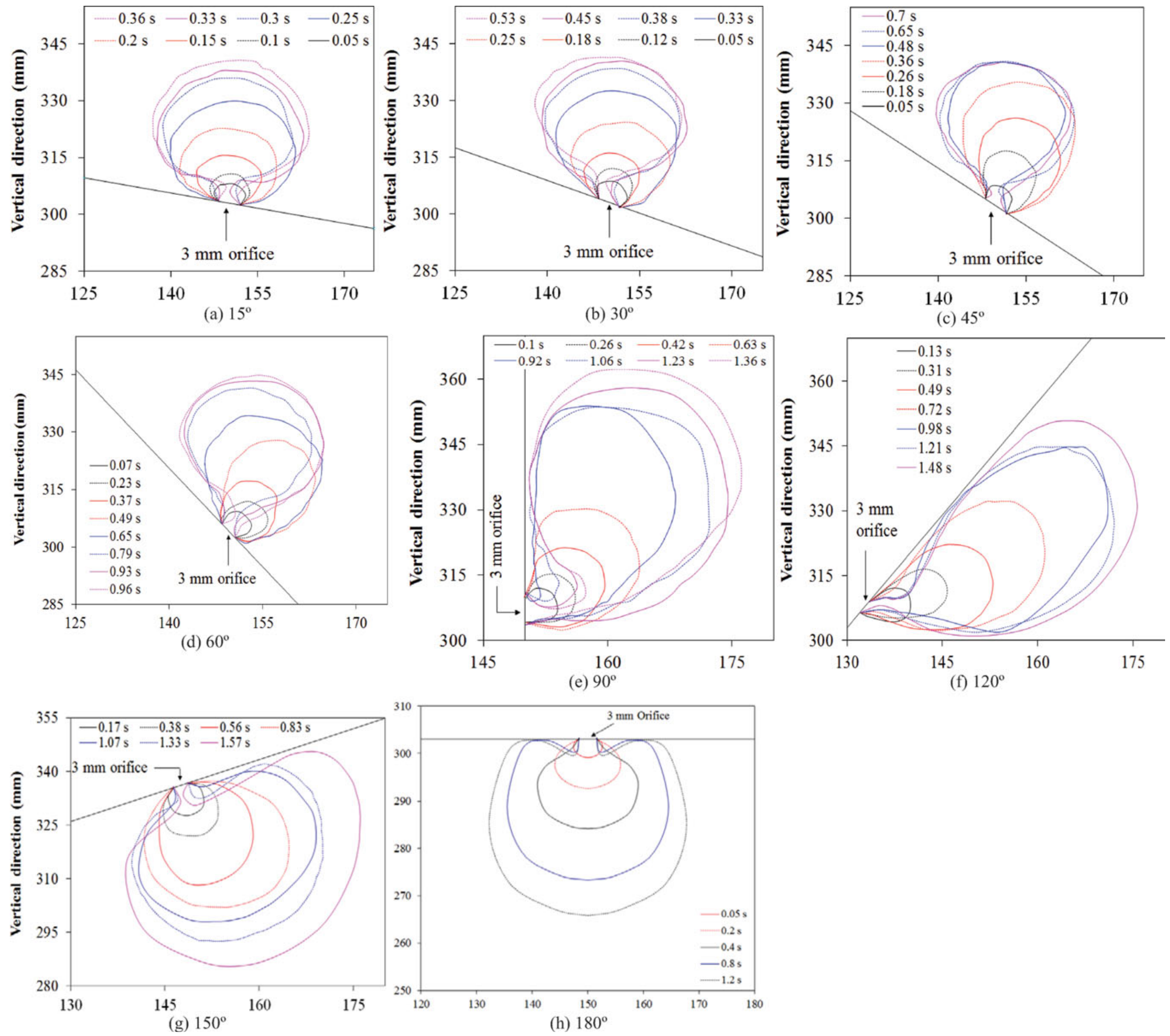
(a) 15°
(b) 30°
(c) 45°
(d) 60°
(e) 90°
(f) 120°
(g) 150°
(h) 180°

Figure 3. Bubble contours at inclined orifices.

[Color figure can be viewed in the online issue, which is available at wileyonlinelibrary.com.]

effect of inclination on the process of bubbling over the full range of inclination. The orifice diameter is taken as 3 mm and the flow rate is considered to be fixed at 30 cm^3/s. For all the inclinations, the approximate height of the free surface is 150 mm above the orifice mouth. Muller and Prince[50] studied the effect of pool height and gas velocity on the type of bubble produced and provided a regime map for different bubbles. The results of present simulation fall within the perfect bubble range proposed by them. Orifice plate inclination is varied in steps starting from 0° to 180°. Figures 3a–h show the bubble contour at orifice mouth at different time steps for inclination of 15°, 30°, 45°, 60°, 90°, 120°, 150°, and 180°, respectively.

The process of bubbling through a submerged orifice is a complex hydrodynamic phenomenon which experiences interplay of a number of forces. These forces vary considerably during the growth of a bubble and render the process highly nonlinear. Almost, all the earlier studies consider a horizontal orifice which reduces the complexity substantially as the bubble retains its axisymmetry till it detaches. An overall force balance presents a system of parallel forces acting on the bubble.

On the contrary, for a tilted orifice, the bubble growth and its initial rise will not be along the orifice axis. The bubble shape as well as the surrounding flow field is 3-D.

When the tilt of the orifice with respect to horizontal plate is small such as 15° as shown in Figure 3a, the asymmetry during bubble growth is marginal. The bubble shapes are also not much different from that observed in the case of a horizontal orifice. As the angle of tilt is increased gradually to 30°, 45°, and 60°, asymmetry in bubble growth becomes prominent. Because of buoyancy, the bubble tends to rise in the vertical direction which is different from the nozzle axis. The bubble boundary is closer to the upper side of the inclined bottom plane particularly at the advanced stages of bubble growth.

The bubble growth from a vertical orifice mouth (angle of inclination 90°) needs a special mention. At the very initial stage of formation, the bubble embryo grows along the nozzle axis which is essentially horizontal. This is due to the

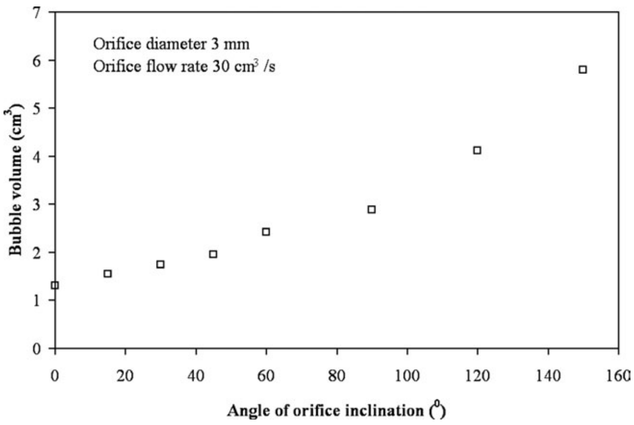

Figure 4. Variation of bubble volume during departure for different orifice inclination.

momentum of the incoming gas stream which is predominantly in a direction mentioned above. As the bubble grows, it cannot defy the effect of gravity for long. As it grows, the bubble aligns itself in the vertical direction. It is interesting to follow the development of the bubble stem or neck. In this particular case, the bubble stem experiences the maximum elongation. Initially, it grows in the horizontal direction but at later stages, it takes a turn in the vertical direction as finally the bubble takes of vertically.

Rest of the figures, till Figure 3h, reveals bubbling from orifice mouth with inclination more than 90°. In these cases, vertical elongation and rise of the bubble will not be possible as the plane of the orifice offers a partial or total obstruction. For an inclination of 120° (Figure 3f), the phenomena are only marginally different from those observed in the case of vertical orifice plate. In this case, at the advanced stage of growth, the bubble boundary comes very close to the plane of the orifice in its effort to rise along a vertical direction. In our simulation, we have not seen the bubble to touch the orifice plane. Also, in this case, the elongation of bubble stem is quite conspicuous.

For an inclination of 150° of the orifice, one can find some change in the scenario. The bubble again regains its ‘‘mushroom shape.’’ However, an overgrowth toward the upper side of orifice plane is obvious particularly at an advanced period of the bubble. Interestingly, a shortening of the bubble stem is noticed. For a downward facing orifice, the bubble grows axisymmetrically with respect to the orifice axis. The bubble stem is small and it does not show any tendency of necking. So, the bubble growth complies with the intuition that increase of bubble volume will give rise to its spreading but no detachment will occur when the orifice plate is mounted on a downward facing plate.

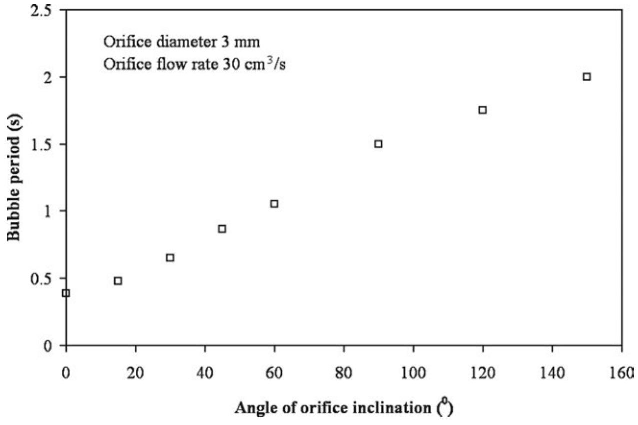

Figure 5. Variation of bubble period for different orifice inclination.

Frequency of bubble formation and bubble volume

In this section, variation of bubble volume at departure and period are investigated for different orifice inclination. Figure 4 shows a monotonic increase in bubble volume at departure with the increase in the orifice inclination. This shows that the bubble release is easier for orifices making acute angle with horizontal than the downward facing orifice plates. For the upward facing orifice, gravity helps in takeoff of the bubble whereas it opposes the detachment for downward facing orifices. One can observe that the rate of increase in bubble volume at departure for different inclination is nonlinear. Bubble volume increases at a much higher rate as the inclination angle approaches 180°. Figure 5 depicts a continuous increase in the bubble growth period and also supports the findings of Figure 4.

Influence of orifice inclination on the asymmetry of the bubble

Bubble formation from an inclined orifice plate is characterized by the asymmetry of the bubble shape. In the case of a horizontal orifice, bubble growth till its departure is axysymmetric, and the center of gravity of the growing bubble shifts only along the axis of the orifice. On the contrary, the center of gravity of a growing asymmetric bubble describes a complex curvilinear trajectory on a vertical plane which passes through the center of the orifice and coincides with the plane of its rotation. The movement of the center of gravity of the bubble is shown in Figure 6.

One of the unique findings of the present investigation is the inception of this asymmetry, its growth, and finally, its termination during the phenomenon of bubbling over the complete range of inclination. A detail account of this is given below.

To make a comparative study of this movement, a vertical axis through the center of the orifice has been taken as the reference for all the inclinations. The position of the moving

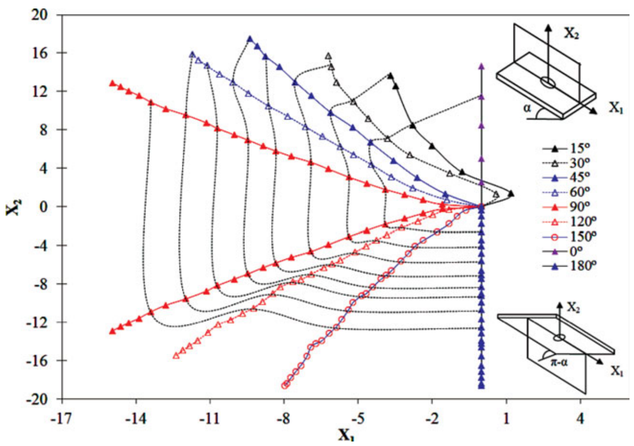

Figure 6. Deviation from symmetric shape for different inclinations of the orifice plate.

[Color figure can be viewed in the online issue, which is available at wileyonlinelibrary.com.]

center of gravity for a typical inclination is indicated by a specific symbol as can be seen from Figure 6. Data points indicate equal time interval of 0.06 s. Furthermore, the position of the center of gravity at a particular instant for all the inclinations has been connected by dotted lines. These lines then are contour lines for equal bubble volume. It may be noted as the orifice is rotated in the clockwise direction over the complete range of inclination, the movement of the bubble center of gravity is restricted grossly in the first and the fourth quadrants.

For a horizontal position of the orifice (inclination of 0°), the bubble center of gravity moves strictly along the vertical line indicating axisymmetry of the bubble with respect to the vertical axis. This has also been reported in earlier numerical investigations.[25] However, it may be noted that in all the earlier numerical investigations, axisymmetry of the bubble was imposed as an assumption. Therefore, one could not be certain whether the axisymmetric bubble shape is a natural attribute of the problem or an outcome of the assumption. The present simulation, conversely, is based on 3-D formulation, and it establishes axisymmetric bubble growth over a horizontal orifice beyond doubt at least for the conditions of simulation.

For a small inclination of the orifice (15°), the deviation of the locus of center of gravity from the vertical line is only marginal. However, the deviation increases with the increase of the inclination indicating the growth of asymmetry. It is interesting to note that though the locus of the center of gravity of a growing bubble deviates from the vertical axis, it can be approximately represented by a straight line for a particular inclination. For instance, for an inclination of 90°, the locus is almost a straight line at an angle of 42° (approximately) with the horizontal. In the case of a horizontal orifice, the growth of the bubble is unrestricted in all the directions above the orifice mouth. The bubble becomes elongated due to the action of gravity as its volume increases. In the case of an inclined orifice, the growing bubble cannot sustain an unrestricted growth. With the growth of the bubble, its left-hand surface approaches the solid plane containing the orifice. The lateral growth of the bubble is then favored in the opposite direction. This results in a shift of the center of the gravity toward the right-hand side of the vertical line.

The bubble growth from a side surface (inclination angle 90°) as shown in Figure 3e needs a special mention. Although the stem is almost horizontal, the shift of the center of gravity is not along a vertical line. This is due to the interplay of a number of conflicting effects. With the bubble growth, its center of gravity moves up. The effect of surface tension is to reduce the surface area. Even in this case, the bubble maintains a minimum distance with the plane of the orifice. In addition, one coordinate system denoted by X_1 (along the orifice plane) and X_2 (perpendicular to the orifice plane) has been defined for each of the inclinations from the center of the orifice.

With inclination as the bubble becomes asymmetric, the center of gravity of the growing bubbles for different inclinations, the center of gravity of the protruded bubble is noticed for the whole period of the bubble. The reference origin for denoting the location of center of gravity is considered to be as the midpoint of the orifice. Two perpendicular axes X_1 and X_2 are framed in a vertical plane aligned with the inclined plate at the orifice mouth. X_1 is aligned with the orifice plate and pointed toward the downward direction while X_2 always points toward top. The system of coordinate axes is mentioned in Figure 6. Based on this coordinate system, the location of the center of mass for different instants of the time period is calculated. Figure 6 shows the location of the center of mass for the whole bubble period for different inclinations of the orifice plate. Points are plotted at an interval of 0.06 s. It can be noticed from the figure that the bubbles are highly asymmetric and center of gravity not remained in the direction of gas flow from the orifice mouth. For an inclination of 15°, the center of mass initially shifts in the positive X_1 direction, but with the progress of time, center of gravity crosses the symmetry line and continues to move toward the left side. At a very small time instant, the gas force dominated over the buoyancy force which causes the center of gravity to shift in the rightward direction. But, with the progress of time, buoyancy takes over making the bubble asymmetric toward left-hand side of X_1–X_2 plane. At the same time, center of gravity also shifts in the upward direction following the X_2 direction. This signifies the growth of the bubble with respect to time. During departure, the bubble center of gravity shows that the shape is totally asymmetric across the symmetry axis (X_2).

With the increase of inclination angle (30°), the asymmetry increases making the center of gravity shift further toward left. During departure, the location of center of gravity is higher for 30° inclination compared to 15° inclination. This causes the increase in bubble volume due to the increase in orifice plate inclination. At 45°, the center of gravity always remained on the left-hand side making the bubble totally asymmetric. The height of the bubble increases further. But, after 45°, the bubble height across the X_2 location decreases but the span in X_1 location increases at a great extent. This can be seen from the location of center of gravity for 60° inclination of the orifice plate. Similar kind of phenomena is also observed for 90° inclination of the orifice plate. At this inclination, the bubble always tries to remain aligned with the vertical orifice plate.

The locations of the center of gravity of bubbles for downward facing orifice plates are determined and plotted in Figure 6. For 120° inclination, it can be observed that though the bubble is upward facing and larger compared to the bubble generated at vertical orifice plate, the asymmetry of the center of gravity reduces. The center of gravity traversed a small offset from the symmetry axis compared to the bubble generated at vertical orifice. But, the height of the bubble across the symmetry axis increases compared to the bubble generated at vertical orifice. At 150° inclination of the orifice plate, the bubble remains downward facing but its symmetry comes back once again. The center of gravity of the bubble shifts a very small distance from the asymmetry axis. This shows that for a totally downward facing bubble (180°), the bubble can be again totally symmetric like upward facing orifice (0°).

Isovolume lines were also plotted in Figure 6 to show that the volume of the bubble during departure increases as the orifice plate becomes more inclined. It can be observed from the figure that the volume of bubble during departure from upward facing orifice is six times less compared to the bubbles departing from 150° inclined orifice.

Vortex structure in the flow field

Figures 7a–e show the velocity vectors of the water and air particles at the vicinity of the bubble during departure for

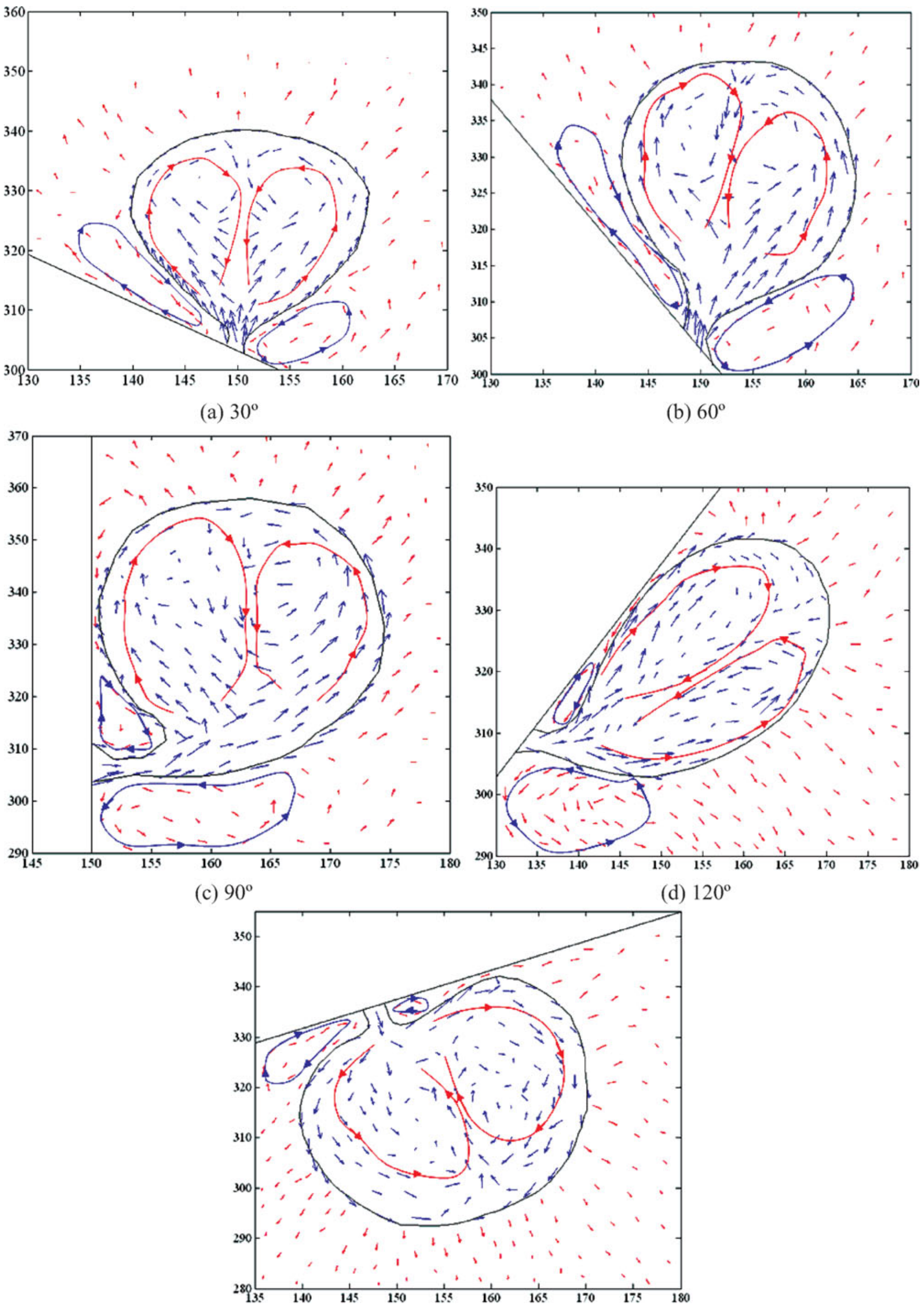

(a) 30°

(b) 60°

(c) 90°

(d) 120°

(e) 150°

Figure 7. Velocity vectors during departure of bubbles at different inclinations.

[Color figure can be viewed in the online issue, which is available at wileyonlinelibrary.com.]

five different inclination of the orifice plate. For all the inclination angle of the orifice plate, vortices are seen inside the gaseous bubble. Primarily, two vortices are seen inside the bubbles. They divide a bubble into two lobes of equal or unequal size. Vortices are also seen in the liquid near the neck region which helps the bubble to detach from the orifice mouth. The velocity vectors of the gaseous particles are denoted by blue arrows while the red arrows denote velocity vectors of the water particles. To demonstrate the dominant vortex structure clearly, we have marked them with red and blue lines, respectively. Arrowheads indicate the corresponding directions of the vortices. At 30° inclination, it can be observed (Figure 7a) that two vortices present inside the bubble during departure are not equal in size. The vortex at the upper region of the bubble is larger compared to the vortex below. Similarly, the vortices in the surrounding liquid are also not symmetric in nature. The vortex at the left-hand side is narrow and long compared to the right-hand side one. This trend continues for the bubble generated at 60° inclination (Figure 7b). The vortices in the liquid side near the neck help the bubble to detach from the orifice mouth.

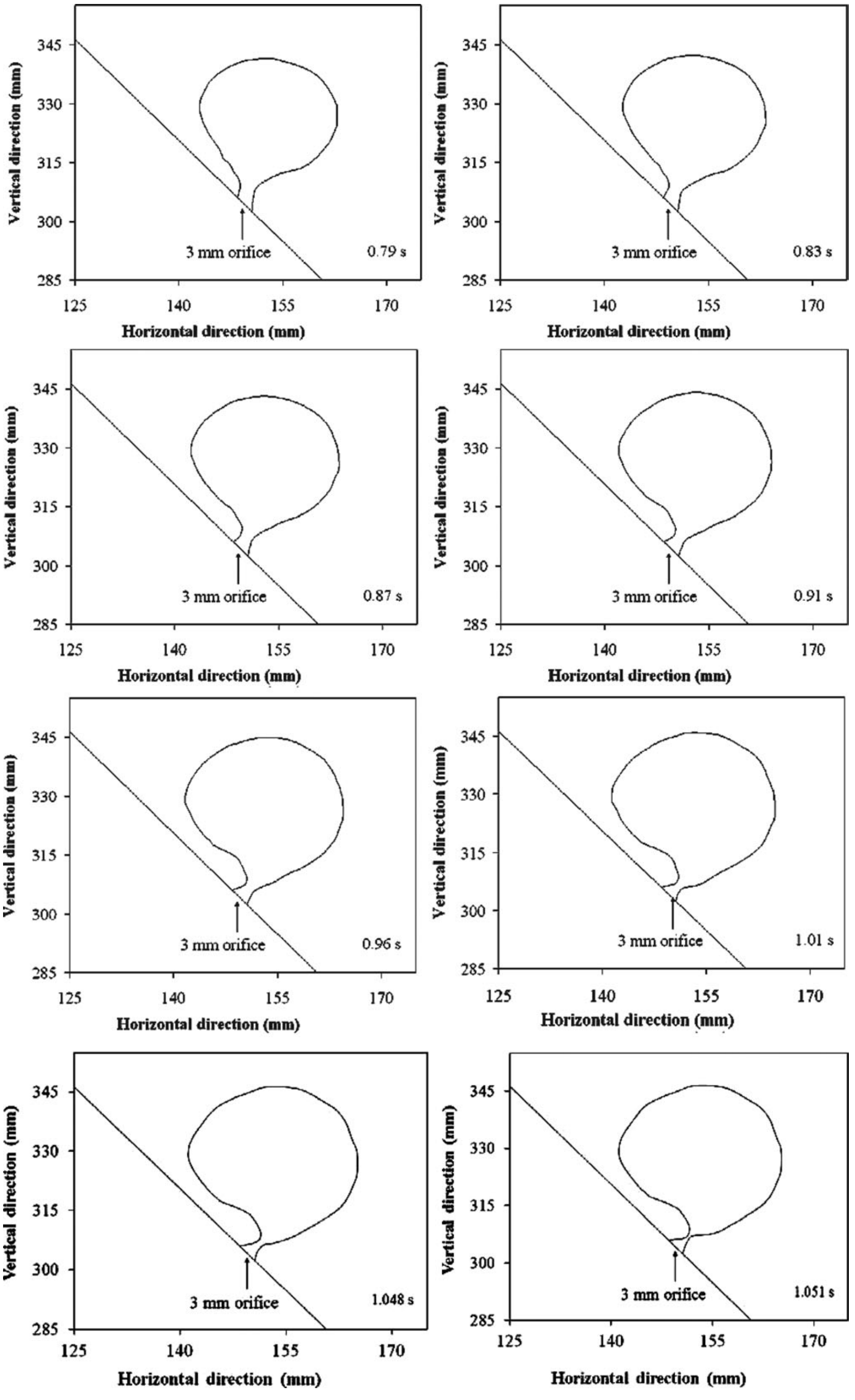

Figure 8. Neck formation at 60° inclination.

For 90° inclination of the orifice plate, the difference between the pair of vortices becomes most prominent (Figure 7c). The vortex near the wall in the gaseous phase is larger. Inside the liquid domain, a small vortex is generated in the entrapped liquid between the bubble and wall. The other vortex far from the vertical wall is much larger and dictates the detachment of the bubble.

For downward facing orifice plates, typical vortex structure can also be noticed from Figures 7d,e. In these two cases, a pair of counter rotating vortices is also present in the air phase. The vortices in the liquid domain are asymmetric. For liquid domain, the upper vortex is quite smaller compared to the lower one. For both the inclinations of 120° and 150°, the lower vortex of the liquid domain

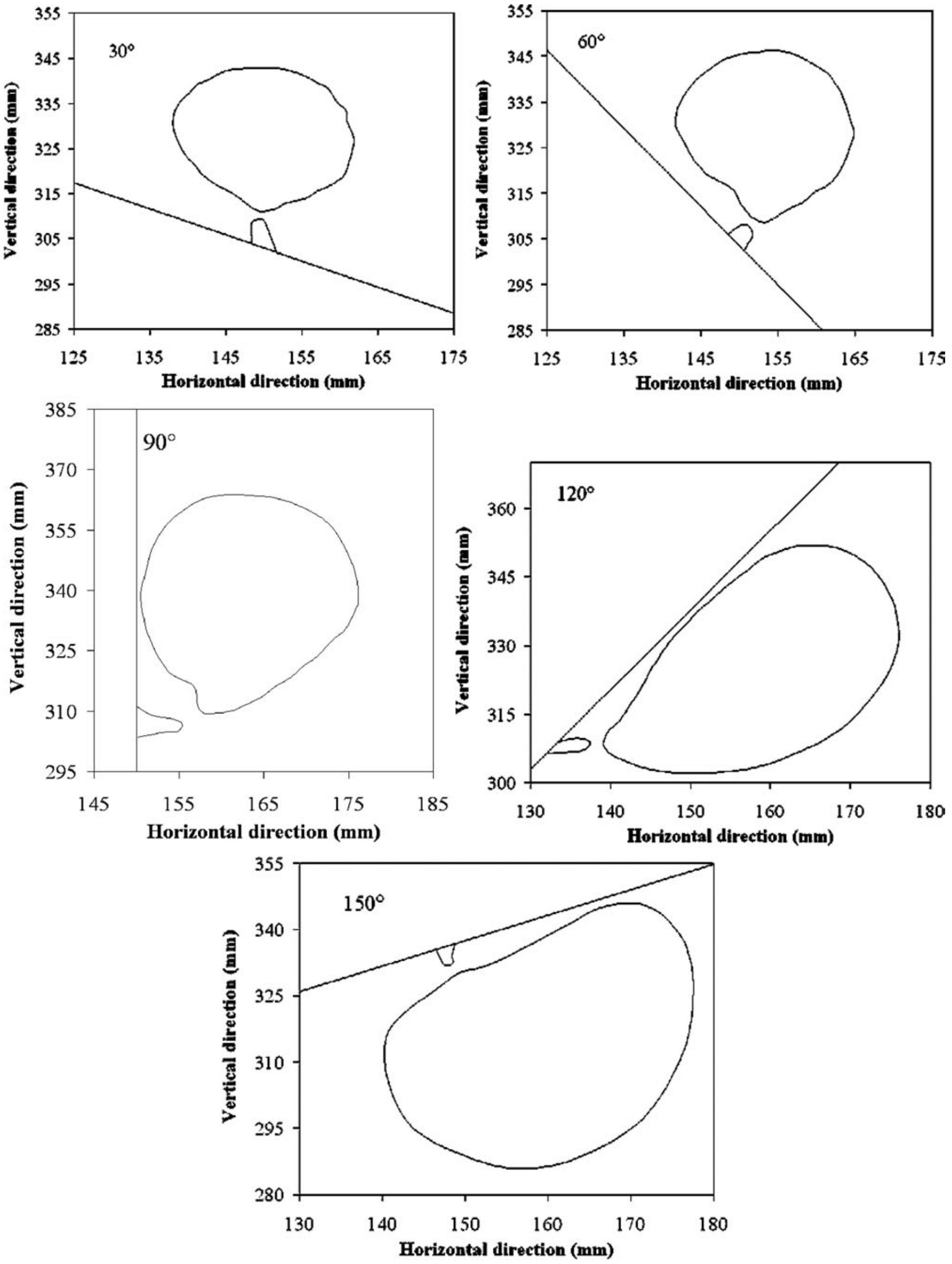

Figure 9. Pinching of bubbles at different inclinations.

controls the detachment and movement of the bubble during departure.

Pinching of bubbles

During the final stage of the growing bubble, the interface near the orifice experiences a negative curvature. This signifies the neck formation. As time progresses, the neck radius decreases making the fronts of the neck region approaching each other. Finally, the neck snaps making the drop detached from the orifice mouth. The time span from the beginning of neck formation till the pinch off of the bubble is termed as necking time. It is observed that the neck is symmetric with respect to the orifice mouth when the orifice plate is vertical. But, as the plate becomes inclined with horizontal, the neck becomes asymmetric. Figure 8 shows the different stages of neck formation and pinching of a bubble over a 60° inclined orifice mouth. From the figure, it is clear that neck is quite asymmetric across the orifice. The formation of neck and its position is influenced by the inclination of the orifice plate with the horizontal (Figure 9). It can be observed from the time contour history of the growing bubbles at the orifice mouth that neck becomes elongated as the orifice plate turns toward vertical. The neck again becomes shallow when the inclination angle increases making the face downward. Conversely, neck location remains above the orifice plane for upward moving orifice plates while it came down the orifice for downward facing plates. In the case of vertical orientation of the orifice plate, the neck remains almost at the same level with the orifice plane.

After detachment of the bubble from the orifice mouth, the bubble tries to move up under the action of buoyancy force. The lower portion of the neck which is attached to the orifice during pinching acts as the embryo of the next bubble. Its shape is mostly governed by the surface tension forces. The

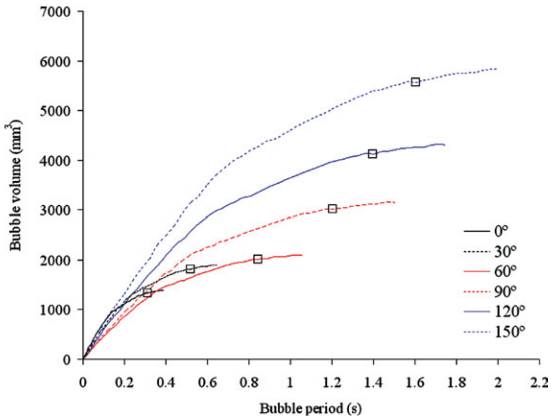

Figure 10. Bubble growth history for different inclinations along with the pinching.

[Color figure can be viewed in the online issue, which is available at wileyonlinelibrary.com.]

embryo keeps the memory of the previous bubble and becomes aligned with the shape of the previous bubble. In Figure 9, we have shown the departing bubble and the remaining gaseous embryo for five different inclination of the orifice plate. It can be observed everywhere that the embryo is offset with the direction of gas flow from the orifice mouth.

Finally, an effort has been made to distinguish between the bubble growth period and the necking period of the bubble over the inclined orifice. Figure 10 shows the bubble growth history for different orifice inclination. From this figure, it is clear that the departure volume and period increase as the orifice becomes more and more inclined from the horizontal orientation. In the same figure, a square marker is also placed to show the point of time at which necking starts for each bubble. The neck formation is delayed as the inclination increases from horizontal to inverted one.

Conclusion

The present investigation was undertaken to study the influence of orifice plate inclination on the bubble formation at a submerged orifice in a quiescent liquid. The significant observations are as follows:

(i) Bubble becomes asymmetric as the orifice plate makes an angle with horizontal plane. Asymmetry increases as the inclination angle increases till the orifice plate becomes vertical (0°→90°). At vertical location (90°), the asymmetry is maximum.

(ii) Asymmetry again reduces and turns toward symmetric shape of the bubble for downward facing orifice plates (>90°). The bubbles more or less follow orifice plate after detachment from the orifice mouth. At 150° inclination, bubble becomes more or less symmetric though its vertex is downward facing.

(iii) The bubble volume during departure and the bubble period increase with the increase of inclination angle of the orifice plate. Buoyancy acts always in the vertically upward direction whereas gas momentum is away from the orifice normal to its plane. The deviation between the lines of action of these two forces increases with the increase in the orifice inclination. The change in bubble volume at departure is an outcome of this.

(iv) Using the history of the traversing for the center of gravity of the bubble for different inclination of the orifice plate, the nature of asymmetry turns out more clear. It shows that the center of gravity always remained at the topside of the line of symmetry from the orifice mouth.

(v) Using the velocity vectors of the particles of both gaseous and liquid phase, it has been shown that vortices are present in both the fluid domain. But, due to the inclination of orifice plate, the vortices become asymmetric. From the velocity vector map, it can be observed that the topmost vortex in the air phase dominates during the bubble growth. Conversely, lower vortex of the liquid domain controls the necking of the bubble from the orifice mouth.

(vi) The process of neck formation is also asymmetric with respect to the orifice mouth. The period of neck formation and the point of time at which neck starts to appear increase as the inclination of the orifice plate increases.

Finally, it can be said that using particle-based numerical methodology, the hydrodynamic structure and interface location of a bubble formation over an inclined orifice are simulated efficiently. It gives a valuable insight regarding the asymmetry present in the bubble structure and its detachment during the process. Developed model can be extrapolated to observe the dynamics of 3-D void in bulk liquid after the pinch off from orifice mouth. This eventually will help to establish the role of orifice inclination for generation of uniform void distribution.

Literature Cited

1. Davidson JF, Schuler BOG. Bubble formation at an orifice in a viscous liquid. *Trans Inst Chem Eng*. 1960;38:144–154.
2. Davidson JF, Schuler BOG. Bubble formation at an orifice in a inviscous liquid. *Trans Inst Chem Eng* 1960;38:335–342.
3. Walters J, Davidson J. The initial motion of a gas bubble formed in an inviscid liquid. *J Fluid Mech*. 1963;17:321–336.
4. McCann DJ, Prince RGH. Bubble formation and weeping at submerged orifice. *Chem Eng Sci*. 1969;24:801–814.
5. Terasaka K, Tsuge H. Bubble formation at a single orifice in highly viscous liquids. *J Chem Eng Jpn*. 1990;23:160–165.
6. Kulkarni AA, Joshi JB. Bubble formation and bubble rise velocity in gas–liquid systems: a review. *Ind Eng Chem Res*. 2005;44:5873–5931.
7. Kim I, Kamotani Y, Ostrach S. Modeling of bubble and drop formation in flowing liquids in microgravity. *AIChE J*. 1994;40:19–28.
8. Pamperin O, Rath HJ. Influence of buoyancy on bubble formation at submerged orifices. *Chem Eng Sci*. 1995;50:3009–3024.
9. Buyevich YA, Webbon BW. Bubble formation at a submerged orifice in reduced gravity. *Chem Eng Sci*. 1996;51:4843–4857.
10. Chakraborty I, Ray B, Biswas G, Durst F, Sharma A, Ghoshdastidar PS. Computational investigation on bubble detachment from submerged orifice in quiescent liquid under normal and reduced gravity. *Phys Fluids*. 2009;21:062103.
11. Ramakrishnan S, Kumar R, Kuloor NR. Studies in bubble formation-I. Bubble formation under constant flow condition. *Chem Eng Sci*. 1969;24:731–747.
12. Marmur A, Rubin E. A theoretical model for bubble formation at an orifice submerged in an inviscid liquid. *Chem Eng Sci*. 1976;31:453–463.
13. Oguz HN, Prosperetti A. Bubble entrainment by the impact of drops on liquid surfaces. *J Fluid Mech*. 1990;219:143–179.
14. Zhang W, Tan RBH. A model for bubble formation and weeping at a submerged orifice. *Chem Eng Sci*. 2000;55:6243–6250.
15. Xiao Z, Tan RBH. An improved model for bubble formation using the boundary integral method. *Chem Eng Sci*. 2005;60:179–186.
16. Quigley CJ, Johnson AI, Harris BL. Size and mass transfer studies of gas bubbles. *Chem Eng Prog Symp Ser*. 1955;16:31–45.
17. Vasilev AS. Laws governing the outflow of a jet of gas into a liquid. *Theo Found Chem Eng*. 1970;4:727.
18. Datta R, Napier DH, Newitt DM. The properties and behaviour of gas bubbles formed at a circular orifice. *Trans Inst Chem Eng*. 1950;28:14–26.
19. Benzing RA, Mayers JE. Low-frequency bubble formation at horizontal circular orifices. *Ind Eng Chem Res*. 1955;47:2087–2090.

20. Liow JL. Quasi-equilibrium bubble formation during top submerged gas injection. *Chem Eng Sci*. 2000;55:4515–4524.
21. Hsu SH, Lee WH, Yang YM, Chang CH, Maa JR. Bubble formation at an orifice in surfactant solutions under constant flow conditions. *Ind Eng Chem Res*. 2000;39:1473–1479.
22. Idogawa K, Ikeda K, Fukuda T, Morooka S. Formation and flow of gas bubbles in a pressurized bubble column with a single orifice or nozzle gas distributor. *Chem Eng Commun*. 1987;59:201–212.
23. Wilkinson PM. Physical aspects and scale-up of high pressure bubble columns. PhD thesis, University of Groningen, 1991.
24. Satyanarayana A, Kumar R, Kuloor NR. Studies in bubble formation—II. Bubble formation under constant pressure conditions. *Chem Eng Sci*. 1969;24:749–761.
25. Antoniadis D, Mantzavinos D. Effect of chamber volume and diameter on bubble formation at plate orifices. *Trans Inst Chem Eng*. 1992;70A:161–165.
26. Leibson I, Holcomb EG, Cacoso AG, Jacmic JJ. Rate of flow and mechanics of bubble formation from single submerged orifices. *AIChE J*. 1956;2:296–300.
27. Tsuge H, Hibino SI. Bubble formation from an orifice submerged in liquids. *Chem Eng Commun*. 1983;22:63–79.
28. Sada E. Bubble formation in molten $NaNO_3$. *Ind Eng Chem Process Des Dev*. 1986;25:838–839.
29. Gerlach D, Biswas G, Durst F, Kolobaric V. Quasi-static bubble formation on submerged orifices. *Int J Heat Mass Transfer*. 2005;48: 425–438.
30. Gerlach D, Alleborn N, Buwa V, Durst F. Numerical simulation of periodic bubble formation at a submerged orifice with constant gas flow rate. *Chem Eng Sci*. 2007;62:2109–2125.
31. Buwa VV, Gerlach D, Durst F, Schlucker E. Numerical simulation of bubble formation on submerged orifices: period-1 and period-2 bubbling regimes. *Chem Eng Sci*. 2007;62:7119–7132.
32. Das AK, Das PK. Bubble evolution through submerged orifice using smoothed particle hydrodynamics: basic formulation and model validation. *Chem Eng Sci*. 2009;64:2281–2290.
33. Das AK, Das PK. Bubble evolution through submerged orifice using smoothed particle hydrodynamics: effect of different thermo physical properties. *Ind Eng Chem Res*. 2009;48:8726–8735.
34. Mandin, P, Aissa AA, Roustan H, Hamburger J, Picard G. Two-phase electrolysis process: from the bubble to the electrochemical cell properties. *Chem Eng Process Process Intensification*. 2008;47:1926–1932.
35. Mandin P, Wuthrich R, Roustan H. Electrochemical engineering modelling of the electrodes kinetic during two-phase sustainable electrolysis. *Comput Aided Chem Eng*. 2009;27:435–440.
36. Mandin P, Wuthrich R, Roustan H. Polarization curves for an alkaline water electrolysis at a small pin vertical electrode to produce hydrogen. *Am Inst Chem Eng J*. 2010;56:2446–2454
37. Marshall SH, Chudacek MW, Bagster DF. A model for bubble formation from an orifice with liquid cross-flow. *Chem Eng Sci*. 1993;48:2049–2059.
38. Forrester SE, Rielly CD. Bubble formation from cylindrical flat and concave sections exposed to a strong liquid cross-flow. *Chem Eng Sci*. 1998;53:1517–1527.
39. Zhang W, Tan RBH. A model for bubble formation and weeping at a submerged orifice with liquid cross-flow. *Chem Eng Sci*. 2003;58:287–295.
40. Kumar R, Kuloor NR. *The formation of bubbles and drops*. In *Advances in Chemical Engineering*. New York: Academic Press, 1970:255–368, Vol. 8.
41. Jacqmin D. Contact-line dynamics of a diffuse fluid interface. *J Fluid Mech*. 2000;402:57–88.
42. Anderson DM, McFadden GB, Wheeler AA. Diffuse-interface methods in fluid mechanics. *Annu Rev Fluid Mech*. 1998;30:139–165.
43. Ding H, Spelt PDM. Inertial effects in droplet spreading: a comparison between diffuse-interface and level-set simulations. *J Fluid Mech*. 2007;576:287–296.
44. Zheng HW, Shu C, Chew YT. A lattice Boltzmann model for multiphase flows with large density ratio. *J Comput Phys*. 2006;218:353–371.
45. Xu Z, Meakin P, Tartakovsky AM. Diffuse-interface model for smoothed particle hydrodynamics. *Phys Rev E*. 2009;79:036702.1–7.
46. Monaghan JJ, Gingold RA. Shock simulation by the particle method SPH. *J Comput Phys*. 1983;52:374–389.
47. Morris JP, Fox JP, Yi Z. Modeling low Reynolds number incompressible flows using SPH. *J Comput Phys*. 1997;136:214–226.
48. Zhang L, Shoji M. A periodic bubble formation from a submerged orifice. *Chem Eng Sci*. 2001;56:5371–5381.
49. Jamialahmadi M, Zehtaban MR, Müller-Steinhagen H, Sarrafi A, Smith JM. Study of bubble formation under constant flow conditions. *Chem Eng Res Des*. 2001;79:523–532.
50. Muller R, Prince RGH. Regimes of bubbling and jetting from submerged orifices. *Chem Eng Sci*. 1972;27:1583–1592.

Annexure 1

SPH methodology replaces the continuum approach by the discrete particle approach through kernel approximation and particle approximation. Using both this approximations, one parameter f_i can be written as

$$f_i = \sum_{j=1}^{N} \frac{m_j}{\rho_j} f_j W(x_i - x_j, h). \tag{A11}$$

For a compact support domain, first- and second-order derivatives can be replaced as

$$f_{xi} = \sum_{j=1}^{N} \frac{m_j}{\rho_j} f_j \frac{\partial W}{\partial x}\bigg|_{(x_i - x_j, h)} \tag{A12}$$

$$f_{xxi} = \sum_{j=1}^{N} \frac{m_j}{\rho_j} f_j \frac{\partial^2 W}{\partial x^2}\bigg|_{(x_i - x_j, h)} \tag{A13}$$

Annexure 2

Stress tensor in the momentum equation includes pressure gradient and viscous stress parameters. Using SPH methodology as described in Annexure 1, it can be defined as

$$\sigma_i^{\alpha\beta} = -p_i \delta^{\alpha\beta} + \mu_i \left(\frac{\partial {v_i}^{\beta}}{\partial {x_i}^{\alpha}} + \frac{\partial {v_i}^{\alpha}}{\partial {x_i}^{\beta}} - \frac{2}{3} (\nabla v_i) \delta^{\alpha\beta} \right) \tag{A21}$$

where ξ_{ij} is the Neumann–Richtmyer artificial viscosity and can be evaluated following Monaghan and Gingold[46]:

$$\xi_{ij} = \begin{cases} \dfrac{-\left(c_i + c_j\right) \sum_j \frac{h v_{ij} x_{ij}}{x_{ij}^2 + \eta^2} + 2 \left(\sum_j \frac{h v_{ij} x_{ij}}{x_{ij}^2 + \eta^2} \right)^2}{\rho_i + \rho_j} & \text{for} \quad v_{ij}.x_{ij} < 0 \\ 0 & \text{for} \quad v_{ij}.x_{ij} \geq 0 \end{cases} \tag{A22}$$

Here, $\eta^2 = 0.001\ \mathrm{h}^2$, v_{ij}, and x_{ij} are the relative velocity and distance of two particles i and j.

Following Annexure 1, chemical potential, ϕ_i and Cahn–Hilliard equation can be written as

$$\begin{aligned} \phi_i = \sum_{j=1}^{N} \frac{m\cdot_j}{\rho_i \rho_j} \frac{\left((C_i + 1)^2 (C_i - 1)^2 - \left(C_j + 1\right)^2 \left(C_j - 1\right)^2 \right)}{\left| r_{ij} \right|} \\ \times \frac{\partial W_{ij}}{\partial r_{ij}} - \sum_{j=1}^{N} \frac{m\cdot_j}{\rho_i \rho_j} \frac{\left(Cn_i^2 + Cn_j^2 \right) \left(G_i - G_j \right)}{\left| r_{ij} \right|} \frac{\partial W_{ij}}{\partial r_{ij}} \end{aligned} \tag{A23}$$

where

$$G_i = \sum_{j=1}^{N} \frac{m\cdot_j}{\rho_i \rho_j} \frac{\left(C_i - C_j \right)}{\left| r_{ij} \right|} \frac{\partial W_{ij}}{\partial r_{ij}} \tag{A24}$$

and

$$\frac{dC_i}{dt} = \sum_{j=1}^{N} \frac{m_j}{\rho_i \rho_j} \frac{(k_i + k_j)\left(\psi_i - \psi_j\right)}{|r_{ij}|} \frac{\partial W_{ij}}{\partial r_{ij}}$$

$$\text{where} \quad \psi_i = \sum_{j=1}^{N} \frac{m_j}{\rho_i \rho_j} \frac{(\phi_i - \phi_j)}{|r_{ij}|} \frac{\partial W_{ij}}{\partial r_{ij}} \tag{A25}$$

Annexure 3

Apart from the bulk momentum transfer, surface tension force is applied across the DI following the CSF method.[47] Using particle-based formulation surface force per unit volume, Fsi can be defined as

$$F_{si} = -\sigma_{lv} \sum_{j=1}^{N} \frac{m_j}{\rho_i \rho_j} \frac{(G_i - G_j)}{|r_{ij}|} \frac{\partial W_{ij}}{\partial r_{ij}} \frac{n}{|n|_s} \delta_s \tag{A31}$$

here δ_s is the interface delta function which assumes finite value only at the interfacial domain. Interfacial surface normal, n can be calculated as

$$n = \sum_{j=1}^{N} \frac{m_j}{\rho_i \rho_j} \frac{(C_i - C_j)}{|r_{ij}|} \frac{\partial W_{ij}}{\partial r_{ij}}. \tag{A32}$$

Moreover, to restrict abrupt mixing of particles across the interface, Lennard–Jones-type resistive force is applied. It can be expressed as

$$F(R) = D\left[\left(\frac{r_0}{r_{ij}}\right)^{12} - \left(\frac{r_0}{r_{ij}}\right)^{6}\right]\frac{x_{ij}}{r_{ij}^2} \quad \text{for } r_{ij} < \mathrm{r}_0$$

$$= 0 \quad \text{for } r_{ij} \geq \mathrm{r}_0 \tag{A33}$$

Here, r_{ij} is the scalar distance between the boundary particle and the fluid particle. r_0 is the minimum spacing of the particles. D is an empirical constant and is assumed to be 15 g times the initial spacing of the particles after rigorous optimality test. The time step is selected such that the physical rate of propagation of information is less than the numerical propagation rate.

Manuscript received Aug. 21, 2011, revision received Feb. 21, 2012, and final revision received Apr. 20, 2012.